MIT Libraries | DSpace@MIT

MIT Open Access Articles

Robust yaw stability controller design and hardware-in-the-loop testing for a road vehicle

Massachusetts Institute of Technology

Robust Yaw Stability Controller Design and Hardware-in-the-Loop Testing for a Road Vehicle

Bilin Aksun Güvenç, *Member, IEEE*, Levent Güvenç, *Member, IEEE*, and Sertaç Karaman

Abstract—Unsymmetrical loading on a car like μ-split braking, side wind forces, or unilateral loss of tire pressure results in unexpected yaw disturbances that require yaw stabilization either by the driver or by an automatic driver-assist system. The use of two-degrees-of-freedom control architecture known as the model regulator is investigated here as a robust steering controller for such yaw stabilization tasks in a driver-assist system. The yaw stability-enhancing steering controller is designed in the parameter space to satisfy a frequency-domain mixed sensitivity constraint. To evaluate the resulting controller design, a real-time hardware-in-the-loop simulator is developed. Steering tests with and without the controller in this hardware-in-the-loop setup allow the driver to see the effect of the proposed controller to improve vehicle-handling quality. The hardware-in-the-loop simulation setup can also be used for real-time driver-in-the-loop simulation of other vehicle control systems.

Index Terms—Hardware-in-the-loop simulation, model regulator, robust control, yaw stability control.

I. INTRODUCTION

DANGEROUS yaw motions of an automobile result from unexpected yaw disturbances that are caused by unsymmetrical car dynamic perturbations like the unilateral loss of tire pressure or braking on a unilaterally icy road called μ-split braking. Safe driving requires a driver to react extremely quickly in such dangerous situations. This is not possible, as the driver who can be modeled as a high gain control system with dead time overreacts, resulting in instability. Consequently, the improvement of automobile yaw dynamics by active control to avoid such catastrophic situations has been and is continuing to be a subject of active research.

The commercially available solution to this problem uses individual wheel braking [1] due to the ease of implementation through the antilock braking system (ABS) actuators. This ease of implementation is enhanced with the recent commercial availability of brake-by-wire systems [2]. Designing individual

B. Aksun Güvenç and L. Güvenç are with the Department of Mechanical Engineering, Istanbul Technical University, Istanbul, Turkey (e-mail: guvencb@itu.edu.tr; guvencl@itu.edu.tr).

S. Karaman is with the Laboratory for Information and Decision Systems, Massachusetts Institute of Technology, Cambridge, MA 02139 USA (e-mail: sertac@mit.edu).

wheel braking controllers that accommodate tire force saturation and coupling between braking and steering in cornering maneuvers improves the capabilities of yaw stability control [3]. During a yaw stabilization maneuver, however, the driver of a car not only applies the brakes but also tries to steer the car. This second approach of using steering for yaw disturbance rejection is treated in this paper. Steering control has been treated in a large number of references, including [4] and [5]. Integrated control of steering and braking has also received a lot of attention in recent years [6]–[10]. Hardware implementation of steering controllers will be much easier when steer-by-wire systems become commercially available. In steer-by-wire systems, the steering wheel is no longer mechanically connected to the tires [11], [12]. The steering-wheel commands are electrically transmitted to the steer-by-wire actuator, which laterally moves the tires. Only the steer-by-wire controller code has to be changed to modify a steering controller. The presence of a steer-by-wire system is assumed here.

The typical presence of large amounts of uncertainty in vehicle steering control for yaw stability enhancement mandates the use of a robust controller. Uncertainty, for example, occurs in the road–tire friction coefficient and the vehicle mass. The large variations in the longitudinal velocity and the dependence of the models that are used on this parameter result in a parameter-varying model that requires a velocity scheduled implementation. It is also desired to use a steering-based yaw stability controller that is easy to tune. Consequently, a robust steering controller based on the model regulator is proposed here, as it has been seen to successfully fulfill similar requirements in earlier work by the authors [13], [14]. A design approach based on mapping frequency-domain performance criteria to model the regulator parameter space is introduced in this paper. Explicit formulas are obtained for basic choices of model regulator filters. An interactive program is used to obtain multiobjective solution regions for the chosen filter parameters.

The single-track model of a vehicle models lateral dynamics quite accurately for moderate levels of lateral acceleration. However, the single-track model cannot capture extreme maneuver dynamics [15]. Such extreme maneuvers are important for testing yaw stability controllers. Therefore, a full-vehicle model is also introduced and used in this paper, along with a single-track model. The model regulator-based yaw stability controller developed here is applied to the full-vehicle model to force it to behave like the steady-state of the single-track model, whose handling properties drivers are used to.

The ultimate and final test for a vehicle stability controller is road testing on a test track. Road tests are expensive and
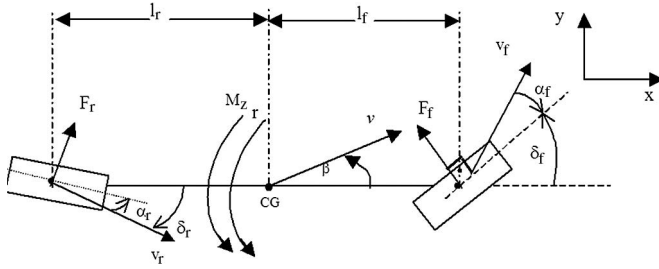
Fig. 1. Single-track model for car steering.

dangerous. Therefore, all major modifications to a vehicle yaw stability controller should be taken care of before road testing, leaving only final checks and fine-tuning. The approach proposed here is to use offline simulations followed by hardware-in-the-loop testing for thorough evaluation before road tests. A hardware-in-the-loop test setup developed for this purpose is introduced in this paper. This hardware-in-the-loop setup allows the evaluation of the control algorithm with the driver in the loop.

The organization of the rest of this paper is as follows. The single-track and full-vehicle models that are used in this paper are given in Section II. The steering actuated yaw stability controller design specifications are given in Section III. The model regulator steering control architecture being used is presented in Section IV. Robust steering controller design is introduced in Section V. A simulation study is given in Section VI. The hardware-in-the-loop test setup that is used for driver-in-the-loop testing is presented in Section VII, where real-time simulation results are also given. This paper ends with conclusions.

II. VEHICLE MODELS USED

A. Single-Track Model

The single-track model, which is also called the bicycle model, is shown in Fig. 1 [16], [17]. The nomenclature used in defining the major variables and geometric parameters of the single-track and full-vehicle models is given in Table I. The nonlinear single-track model is characterized by the steering angle projection (also called the force coordinate transformation)

$$\begin{bmatrix} \sum F_x \\ \sum F_y \\ \sum M_z \end{bmatrix} = \begin{bmatrix} -\sin d_f & -\sin d_r \\ \cos d_f & \cos d_r \\ l_f \cos d_f & -l_r \cos d_r \end{bmatrix} \begin{bmatrix} F_f \\ F_r \end{bmatrix} \quad (1)$$

the dynamics equations

$$\begin{bmatrix} mv(\dot{\beta} + r) \\ m\dot{v} \\ I_z \dot{r} \end{bmatrix} = \begin{bmatrix} -\sin\beta & \cos\beta & 0 \\ \cos\beta & \sin\beta & 0 \\ 0 & 0 & 1 \end{bmatrix} \begin{bmatrix} \sum F_x \\ \sum F_y \\ \sum M_z \end{bmatrix} \quad (2)$$

and the equations of kinematics/geometry

$$\tan\beta_f = \tan\beta + \frac{l_f r}{v\cos\beta} \quad (3)$$

$$\tan\beta_r = \tan\beta - \frac{l_r r}{v\cos\beta}. \quad (4)$$

TABLE I
NOMENCLATURE

Symbol	Description	Unit
m	Total vehicle mass	kg
F_f (F_r)	Lateral wheel force at front (rear) wheel	N
F_{xi} (F_{yi})	Longitudinal (lateral) tire forces	N
F_x (F_y)	Forces in x (y) directions	N
M_z	Moment about the vertical axis z through the center of gravity (CG)	Nm
δ_f (δ_r)	Steering inputs for the single track model	rad
δ_i	Steering inputs	rad
β	Chasis side slip angle at vehicle CG	rad
v_x (v_y)	Velocity in x (y) direction	m/s
a_x (a_y)	Acceleration in x (y) direction	m/s²
x (y)	Position in x (y) direction	m
I_z	Moment of inertia about z axis	kgm²
l_{xi} (l_{yi})	Distance of ith tire to CG along x (y) coordinates	m
l_f (l_r)	Distance from CG to front (rear) axle	m
l_w	Wheel base (axle width)	m
I_t	Tire inertia	m
ω_i	Tire angular velocities	rad/s
R_e	Effective tire radius	m
v	Magnitude of velocity at CG (v>0, dv/dt=0)	m/s
$\vec{v}_1, \vec{v}_2, \vec{v}_3, \vec{v}_4$	Tire center velocities	m/s
$\alpha_1, \alpha_2, \alpha_3, \alpha_4$	Tire side slip angles	rad
s_i	Tire slip	-
C_{xi} (C_{yi})	Longitudinal (lateral) cornering stiffness	N (N/rad)
F_{Zi}	Vertical tire forces	N
F_{Si}	Spring forces	N
F_{Di}	Damper forces	N
m_s	Sprung mass quantity	kg
a_z	Vertical acceleration	m/s²
z	Vertical position of the sprung mass	m
K_{RF}	Front right spring coefficient	N/m
K_{LF}	Front left spring coefficient	N/m
K_{RR}	Rear right spring coefficient	N/m
K_{LR}	Rear left spring coefficient	N/m
B_{RF}	Front right damping rate	N/(m/s)
B_{LF}	Front left damping rate	N/(m/s)
B_{RR}	Rear right damping rate	N/(m/s)
B_{LR}	Rear left damping rate	N/(m/s)
I_x (I_y)	Moment of inertia about x (y) axis	kgm²
t_f (t_r)	Front (rear) wheel base	m
ψ	Yaw angle	rad
Φ	Roll angle	rad
φ	Pitch angle	rad
h_{CG}	Distance from CG to pitch center	m
U_{RF}	Road profile under right front wheel	m
U_{LF}	Road profile under left front wheel	m
U_{RR}	Road profile under right rear wheel	m
U_{LR}	Road profile under left rear wheel	m

The tire longitudinal forces F_f and F_r are nonlinear functions of the corresponding sideslip angles a_f and a_r. F_f and F_r also depend on the friction characteristics between the road and the tires. The nonlinear single-track model is shown in the top part of the block diagram of Fig. 2. A vehicle with front-wheel steering is considered here. Thus, $\delta_r = 0$ in (1).

The variable exhibiting the largest variation in the single-track model is longitudinal velocity v at the vehicle center of mass. It is customary to linearize the single-track model while keeping v as a variable parameter. The resulting model is a linear-parameter-varying one whose operating condition depends on vehicle velocity. It is also customary to design controllers for several velocity values and to use a gain scheduling
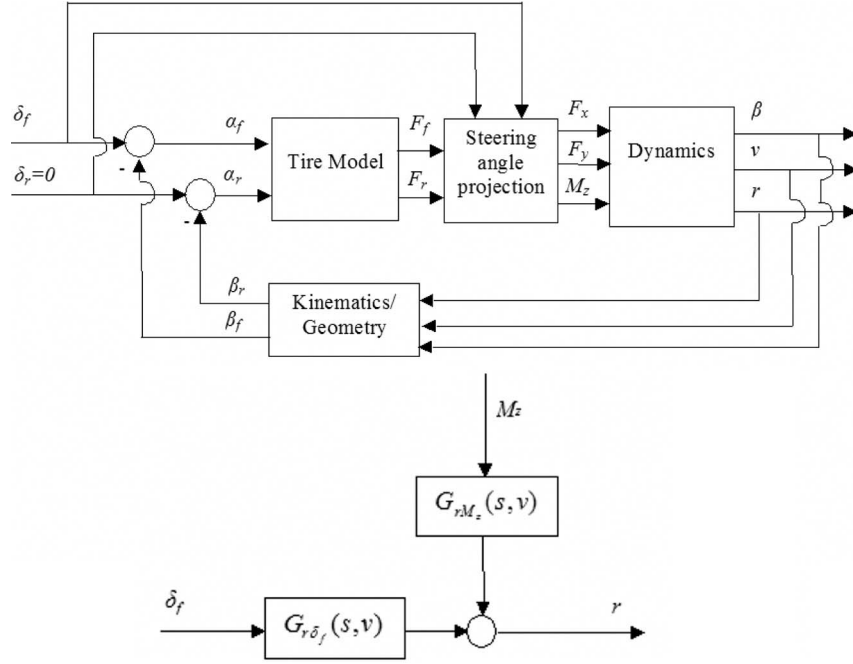
Fig. 2. (Top) Nonlinear and (bottom) linearized single-track model block diagrams.

controller. This approach is used here as well. The nonlinear single-track model is linearized assuming small steering angles δ_f and small sideslip angle β. The tire force characteristics are linearized as

$$F_f(\alpha_f) = \mu c_{f0}\alpha_f = c_f\alpha_f$$
$$F_r(\alpha_r) = \mu c_{r0}\alpha_r = c_r\alpha_r \qquad (5)$$

where c_f and c_r are the tire cornering stiffnesses, μ is the road–tire friction coefficient, and the tire sideslip angles are given by

$$\alpha_f = \delta_f - \left(\beta + \frac{l_f}{v}r\right) \qquad (6)$$

$$\alpha_r = -\left(\beta - \frac{l_r}{v}r\right). \qquad (7)$$

Note that c_{f0} and c_{r0} in (5) are the nominal values for $\mu = 1$ of the tire cornering stiffnesses. The transfer function from front-wheel steering angle δ_f to yaw rate r is given by

$$G_{r\delta_f}(s,v) = \frac{r(s)}{\delta_f(s)} = \frac{b_1(v)s + b_0(v)}{a_2(v)s^2 + a_1(v)s + a_0(v)} \qquad (8)$$

with

$$b_0 = c_f c_r(l_f + l_r)v$$
$$b_1 = c_f l_f m v^2$$
$$a_0 = c_f c_r(l_f + l_r)^2 + (c_r l_r - c_f l_f)m v^2$$
$$a_1 = \left(c_f\left(I_z + l_f^2 m\right) + c_r\left(I_z + l_r^2 m\right)\right)v$$
$$a_2 = I_z m v^2.$$

$G_r\delta_f(s,v)$ in (8) is also called the steering-wheel input response transfer function here. The dc gain of the nominal single-track model (8) is given by

$$K_n(v) = \lim_{s\to 0} G_{r\delta_f}(s,v)\Big|_{\mu=\mu_n=1} \qquad (9)$$

at chosen longitudinal speed v and at nominal friction coefficient $\mu = \mu_n$, which is taken as unity here.

The yaw moment disturbance input response is given by

$$G_{rM_z}(s,v) = \frac{r(s)}{M_z(s)} = \frac{mv^2 s + (c_f + c_r)v}{a_2(v)s^2 + a_1(v)s + a_0(v)}. \qquad (10)$$

The block diagram of the linearized single-track model is shown at the bottom of Fig. 2.

B. Full-Vehicle Model

The full-vehicle model consists of the vehicle body represented as a sprung mass with three degrees of freedom, connected to the tires through suspensions modeled as mass–spring–damper systems. The tires are connected to each other by a double-track model. The full-vehicle model is illustrated in Fig. 3. The equations of motions governing longitudinal and lateral dynamics of the double-track base are given by

$$m(a_x - rv_y) = \sum F_x = \sum_{i=1}^4 (F_{xi}\cos\delta_i - F_{yi}\sin\delta_i) \quad (11)$$

$$m(a_y + rv_x) = \sum F_y = \sum_{i=1}^4 (F_{xi}\sin\delta_i + F_{yi}\cos\delta_i) \quad (12)$$

where $i = 1, 2, 3,$ and 4 refers to individual tires.

The equation of motion around the yaw axis is

$$I_z\dot{r} = \sum M_z = \sum_{i=1}^4 (l_{xi}(F_{xi}\cos\delta_i + F_{yi}\sin\delta_i)$$
$$+ l_{yi}(F_{xi}\sin\delta_i + F_{yi}\cos\delta_i)) + M_d. \quad (13)$$

A vehicle with front-wheel steering is considered here. Thus, $\delta_1 = \delta_2 = \delta_f$, and $\delta_3 = \delta_4 = \delta_r$ in (11)–(13).
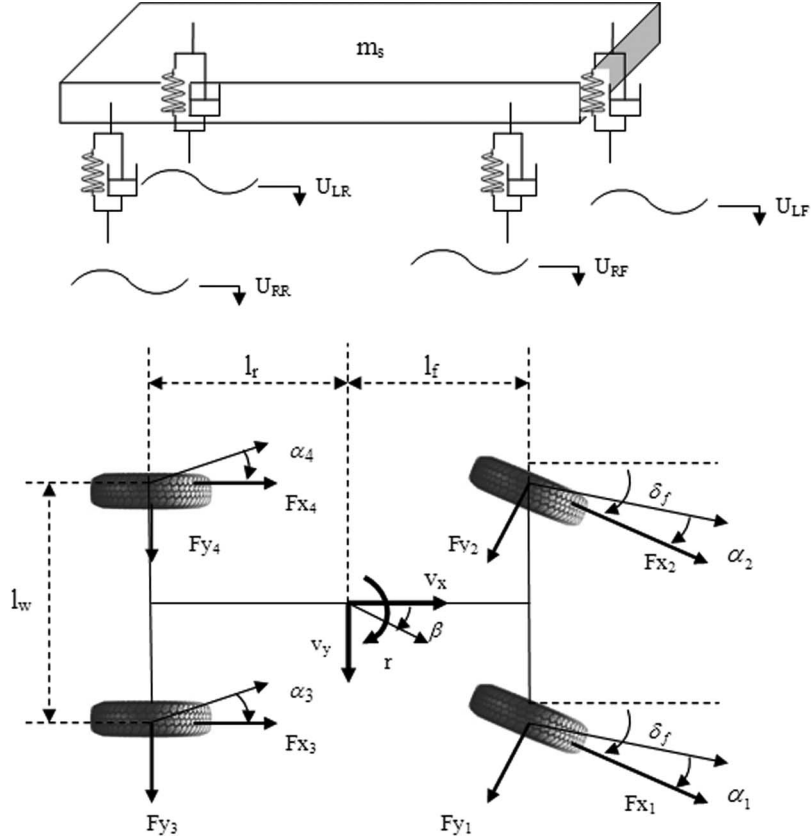
Fig. 3. Full-vehicle model.

The tire rotational dynamics are given by

$$I_t \omega_i = T_i - R_e F_{xi} \tag{14}$$

and the tire center velocities are given by

$$\vec{v}\_1 = (v_x - r(l_w/2))\,\vec{i} + (v_y + rl_f)\vec{j}$$

$$\vec{v}_2 = (v_x + r(l_w/2))\,\vec{i} + (v_y + rl_f)\vec{j}$$

$$\vec{v}_3 = (v_x - r(l_w/2))\,\vec{i} + (v_y - rl_f)\vec{j}$$

$$\vec{v}_4 = (v_x + r(l_w/2))\,\vec{i} + (v_y - rl_f)\vec{j} \tag{15}$$

where $\vec{i}$ and $\vec{j}$ are the unit vectors in the x- and y-directions, respectively. The tire sideslip angles are

$$\alpha_1 = -\delta_f + \tan^{-1}\left(\frac{v_y + rl_f}{v_x - r(l_w/2)}\right)$$

$$\alpha_2 = -\delta_f + \tan^{-1}\left(\frac{v_y + rl_f}{v_x + r(l_w/2)}\right)$$

$$\alpha_3 = \tan^{-1}\left(\frac{v_y - rl_r}{v_x - r(l_w/2)}\right)$$

$$\alpha_4 = \tan^{-1}\left(\frac{v_y - rl_r}{v_x + r(l_w/2)}\right) \tag{16}$$

and the longitudinal wheel slip ratio is defined as

$$s_i = \begin{cases} \frac{R_e\omega_i - V_{xi}}{V_{xi}}, & R_e\omega_i < V_{xi} \text{ (braking)} \\ \frac{R_e\omega_i - V_{xi}}{R_e\omega_i}, & R_e\omega_i > V_{xi} \text{ (traction)}. \end{cases} \tag{17}$$

The Dugoff tire model with

$$F_{xi} = f_i C_{xi} s_i$$

$$F_{yi} = f_i C_{yi} \alpha_i \tag{18}$$

as the longitudinal and lateral tire forces, respectively, is used. The coefficients f_i are calculated using

$$f_i = \begin{cases} 1, & F_{Ri} \leq \frac{\mu_i F_{zi}}{2} \\ \left(2 - \frac{\mu_i F_{zi}}{2F_{Ri}}\right)\frac{\mu_i F_{zi}}{2F_{Ri}}, & F_{Ri} > \frac{\mu_i F_{zi}}{2} \end{cases} \tag{19}$$

$$F_{Ri} = \sqrt{(C_{xi}\sigma_i)^2 + (C_{xi}\alpha_i)^2}. \tag{20}$$

The equation of motion for the vertical dynamics of the sprung mass is

$$m_s a_z = \sum F_z$$

$$a_z = \ddot{z} - \dot{x}\dot{\varphi} + \dot{y}\dot{\Phi}. \tag{21}$$

The forces in the z-direction consist of a summation of spring and damper forces and the weight of the sprung mass given by

$$\sum F_z = m_s g - (F_{S1} + F_{S2} + F_{S3} + F_{S4} \\ + F_{D1} + F_{D2} + F_{D3} + F_{D4}). \quad (22)$$

The spring and damper forces are given by

$$F_{S1} = K_{RF}\left(\delta_f - \frac{t_F}{2}\Phi - l_f\varphi + z + U_{RF}\right)$$

$$F_{S2} = K_{LF}\left(\delta_f - \frac{t_F}{2}\Phi - l_f\varphi + z + U_{LF}\right)$$

$$F_{S3} = K_{RR}\left(-\frac{t_R}{2}\Phi - l_r\varphi + z + U_{RR}\right)$$

$$F_{S4} = K_{LR}\left(-\frac{t_R}{2}\Phi - l_r\varphi + z + U_{LR}\right) \quad (23)$$

$$F_{D1} = B_{RF}\left(\frac{t_F}{2}\dot{\Phi} - l_f\dot{\varphi} + \dot{z} + \dot{U}_{RF}\right)$$

$$F_{D2} = B_{LF}\left(-\frac{t_F}{2}\dot{\Phi} - l_f\dot{\varphi} + \dot{z} + \dot{U}_{LF}\right)$$

$$F_{D3} = B_{RR}\left(\frac{t_R}{2}\dot{\Phi} - l_r\dot{\varphi} + \dot{z} + \dot{U}_{RR}\right)$$

$$F_{S4} = B_{LR}\left(-\frac{t_R}{2}\dot{\Phi} - l_r\dot{\varphi} + \dot{z} + \dot{U}_{LR}\right). \quad (24)$$

Then, the equations of motion regarding the roll and pitch dynamics are, respectively, given as

$$\sum T_{RC} = I_x\ddot{\Phi}$$

$$= m_s g h_{CG}\Phi - m_s(\ddot{y} + \dot{x}\dot{\psi} + -\dot{z}\dot{\Phi})h_{CG}$$

$$- \frac{t_F}{2}(F_{S1} + F_{D1}) + \frac{t_F}{2}(F_{S2} + F_{D2})$$

$$- \frac{t_R}{2}(F_{S3} + F_{D3}) + \frac{t_R}{2}(F_{S4} + F_{D4}) \quad (25)$$

$$\sum T_{PC} = I_y\ddot{\varphi}$$

$$= m_s g h_{CG}\varphi - m_s(\ddot{x} - \dot{y}\dot{\psi} + \dot{z}\dot{\varphi})h_{CG}$$

$$+ (F_{S1} + F_{S2} + F_{D1} + F_{D2})l_f$$

$$- (F_{S3} + F_{S4} + F_{D3} + F_{D4})l_r. \quad (26)$$

Finally, the forces in the z-direction for each tire can be calculated as

$$F_{zi} = F_{Si} + F_{Di} \quad (27)$$

which is fed back to (19) of the tire model, coupling the double-track base and the vertical suspension dynamics.

III. MODEL UNCERTAINTY AND DESIGN SPECIFICATIONS

The two variables exhibiting the largest variation during operation are longitudinal speed v and mass m of the vehicle.
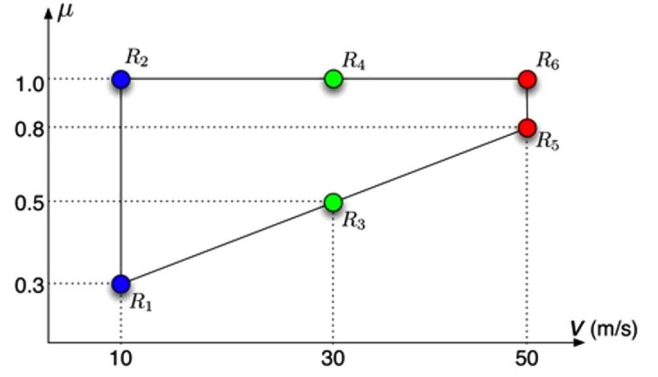

Fig. 4. Uncertainty specifications.

The tire cornering stiffnesses can also exhibit large variations due to variations in the tire–road friction coefficient. In addition to the vehicle model dynamics, there is also the steer-by-wire actuator, whose dynamics should be considered in the simulations. The steering actuator model that is assumed to be under closed-loop position control is modeled as a second-order system with a bandwidth of $\omega_a = 2\pi 15$ rad/s (15 Hz) and a damping ratio of $\zeta_a = 0.7$ as

$$G_{sa} = \frac{\delta_f}{\delta_{\text{ref}}} = \frac{\omega_a^2}{s^2 + 2\zeta_a\omega_a s + \omega_a^2}. \quad (28)$$

The uncertain parameters and their uncertainty ranges will first be given before the design specification. Longitudinal speed v is assumed to vary between a minimum value of 10 m/s and a maximum value of 50 m/s during operation. Note that longitudinal speed v of the vehicle is a measurable quantity. It will be assumed to be measured and will be used in the yaw stability controller implementation introduced later in this paper. The yaw dynamics compensator is assumed to be shut off at speeds below 10 m/s since the driver is easily able to reject yaw disturbances at these speeds without the need for steering controller assistance. Road adhesion factor μ is assumed to exhibit the characteristics displayed in Fig. 4 with velocity. The maximum value of μ is unity at all speeds in this figure, whereas its minimum possible value linearly varies between 0.30 at low speeds and 0.80 at high speeds.

In this study, the operating regions for the vehicle are based on the values of the vehicle longitudinal speed between 10 and 50 m/s. Six exemplary operating points have been chosen and are shown with large dots having separate labels and color coding in Fig. 4. The aim in steering compensator design is to make sure that, first, stable operation, and then improved yaw dynamics, are achieved for all operating regions and all possible values of the uncertain parameters. The improved yaw dynamics corresponds to good disturbance rejection properties, where the possible disturbances include the effect of side wind forces, tire rupture, unsymmetrical brake wear, and μ-split braking. The steering-wheel input response in the absence of disturbances should also be well damped, regardless of the speed of operation. A model regulator-based steering controller is designed and shown to effectively achieve the desired aims in the following sections.
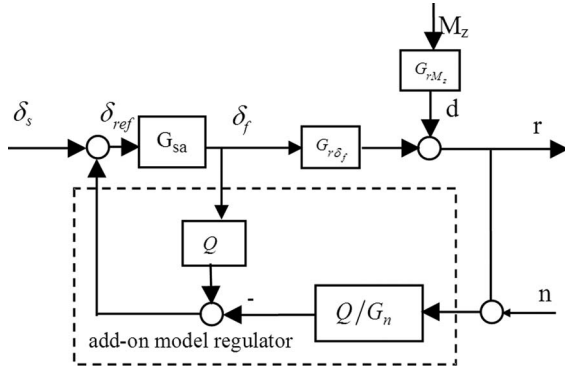
Fig. 5.   Steer-by-wire system with a model regulator.

IV. MODEL REGULATOR ARCHITECTURE

A review of model regulator basics is given in this section (see [18]–[21]). Referring to Fig. 5, the vehicle model can also be expressed as

$$r = G_{r\delta_f}\delta_f + d = (G_n(1 + \Delta_m))\,\delta_f + d \qquad (29)$$

where $G_r\delta_f = G_n(1 + \Delta_m)$ is the actual input–output relation between front-wheel steering angle δ_f and vehicle yaw rate r. Δ_m is the multiplicative model uncertainty in our knowledge of nominal model G_n, and d is the external disturbance. The location of steering actuator transfer function G_{sa} in Fig. 5 corresponds to a steer-by-wire system. The aim in the model regulator steering controller design is to approximately obtain

$$\frac{r}{\delta_s} = G_n G_{sa} \qquad (30)$$

as the input–output relation (the steering transfer function) despite the presence of model uncertainty Δ_m and external disturbance d. δ_s is the steering-wheel angle input by the driver. Rewrite (29) as

$$r = G_n\delta_f + (G_n\Delta_m\delta_f + d) = G_n\delta_f + e \qquad (31)$$

by defining the extended disturbance e and solving for it as

$$e = r - G_n\delta_f. \qquad (32)$$

The control law

$$\delta_f = G_{sa}\delta_s - G_n^{-1}e = G_{sa}\delta_s - G_n^{-1}r + \delta_f \qquad (33)$$

where the expression in (32) for e has been substituted for on the right-hand side will result in aim (30) when substituted in the dynamics given by (31). The control law in (33) cannot be implemented, as it is not causal since δ_f appears on both sides and since G_n^{-1} will not be a proper transfer function. Feedback signals also have to go through steering actuator dynamics G_{sa} in a real implementation. All of these problems are solved by multiplying the feedback signals in (33) by unity dc gain low-pass filter Q and steering actuator dynamics filter G_{sa}, resulting in the following model regulator implementation equation:

$$\delta_f = G_{sa}\left(\delta_s - QG_n^{-1}r + Q\delta_f\right) \qquad (34)$$

which is shown in Fig. 5 within the dashed rectangle. The relative degree of unity dc gain low-pass filter Q is chosen to be at least equal to the relative degree of G_n for causality of Q/G_n. The structure of Q is assumed to be

$$Q = \frac{1}{\tau_Q s + 1}. \qquad (35)$$

Note that this choice will result in an integrator within the loop in Fig. 5 and, hence, zero steady-state error in response to step steering commands and yaw torque disturbances [14].

The nominal (or desired) yaw dynamic model is chosen as a first-order system given by

$$G_n(s, v) = \frac{K_n(v)}{\tau_n s + 1} \qquad (36)$$

where $K_n(v)$ is the dc gain of the nominal single-track model at the chosen longitudinal speed v. The aim in the choice of (36) for desired steering dynamics G_n is to force the controlled system to possess the behavior of the single-track model within the bandwidth of Q. A nonovershooting first-order dynamics is also imposed for faster response. Vehicle velocity v is a measurable variable. It is, therefore, used in the controller in (36), as $K_n(v)$ in that equation is the velocity-dependent static gain of the bicycle or single-track model. The dependence of G_n on vehicle velocity v makes the controller continuously velocity-scheduled. Note that the yaw dynamics of a vehicle, as represented by its bicycle or single-track model, change with vehicle velocity v. The continuous gain scheduling approach that is used allows the adaptation of the controller to these changes.

According to (29) and (36), model uncertainty Δ_m is given by

$$\Delta_m = \frac{G_{r\delta_f} - G_n}{G_n} = \frac{G_{r\delta_f}(s,v)(\tau_n s + 1)}{K_n(v)} - 1 \qquad (37)$$

and is parameter varying, as it depends on the measurable speed of the vehicle.

The open-loop gain of the model regulator-compensated yaw dynamics model is given by

$$L = \frac{G_{r\delta_f}G_{sa}Q}{G_n(1 - G_{sa}Q)} \qquad (38)$$

where the model regulation, disturbance rejection, and sensor noise rejection transfer functions are given by

$$\frac{r}{\delta_s} = \frac{G_n G_{sa} G_{r\delta_f}}{G_n(1 - G_{sa}Q) + G_{sa}G_{r\delta_f}Q} \qquad (39)$$

$$\frac{r}{d} = \frac{1}{1 + L} := S = \frac{G_n(1 - G_{sa}Q)}{G_n(1 - G_{sa}Q) + G_{sa}G_{r\delta_f}Q} \qquad (40)$$

$$-\frac{r}{n} = \frac{L}{1 + L} := T = \frac{G_{sa}G_{r\delta_f}Q}{G_n(1 - G_{sa}Q) + G_{sa}G_{r\delta_f}Q}. \qquad (41)$$

S in (40) is the sensitivity function, and T in (41) is the complementary sensitivity function of the controlled system. It is obvious from (39)–(41) that for good performance, Q must be a unity gain low-pass filter (G_{sa} is a unity gain low-pass filter as well). This choice will result in $r/\delta_s \to G_n$ (model regulation), $r/d \to 0$ (disturbance rejection) at low frequencies, where $Q \to 1$, and $r/n \to 0$ (sensor noise rejection) at high
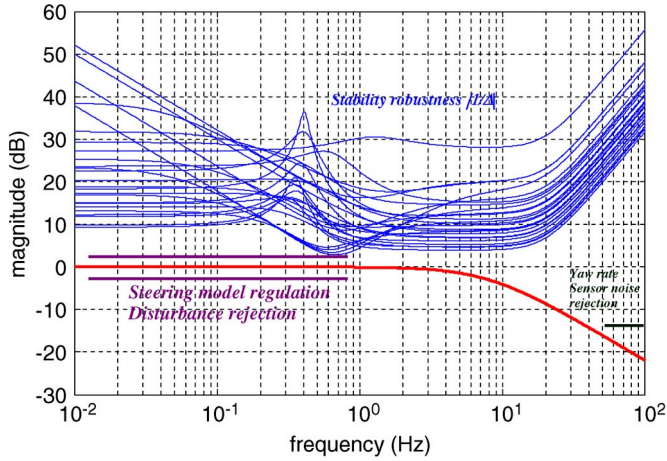
Fig. 6. Steering model regulator design requirements.

frequencies, where $Q \to 0$, as is desired. The model regulator design is, thus, shaping filter Q to satisfy the design objectives. The first limitation on the bandwidth of Q comes from the sensor noise rejection at sensor noise frequencies. The second limitation is that the bandwidth of Q should not be larger than the bandwidth of the actuator used, as it makes no sense to command what cannot be achieved.

A. Stability and Stability Robustness Analysis

Checking the stability of the model regulator control system when there is no uncertainty is a simple stability check, where

$$\text{Re}\{\text{roots}(1 + L = 0)\} < 0 \quad \text{or}$$
$$\text{Re}\{\text{roots}\left(G_n(1 - G_{sa}Q) + G_{sa}G_{r\delta_f}Q = 0\right)\} < 0 \quad (42)$$

needs to be satisfied; that is, all roots of the characteristic equation must lie in the left half-plane. Robustness of stability is more important for the model regulator control system and results in another bandwidth limitation for the Q filter. The characteristic equation for the model regulator control loop is given by

$$G_n\left[(1 - G_{sa}Q) + G_{sa}(1 + \Delta_m)Q\right]$$
$$= G_n(1 + G_{sa}\Delta_m Q) = 0 \quad (43)$$

which is equivalent to

$$(1 + G_{sa}\Delta_m Q) = (1 + \Delta Q) = 0, \quad \Delta \equiv G_{sa}\Delta_m \quad (44)$$

since G_n is stable, or

$$|\Delta| \equiv |G_{sa}\Delta_m| < \left|\frac{1}{Q}\right| \quad \forall \omega \quad (45)$$

as a sufficient condition for stability robustness in the presence of unstructured multiplicative model uncertainty Δ_m in the plant. As long as unstructured model uncertainty Δ_m in the plant obeys inequality (45), the robustness of stability is guaranteed. This is graphically illustrated in Fig. 6, where Q and $1/\Delta$ are shown instead of their inverses as in (45). Please note that in the model regulator control architecture that is
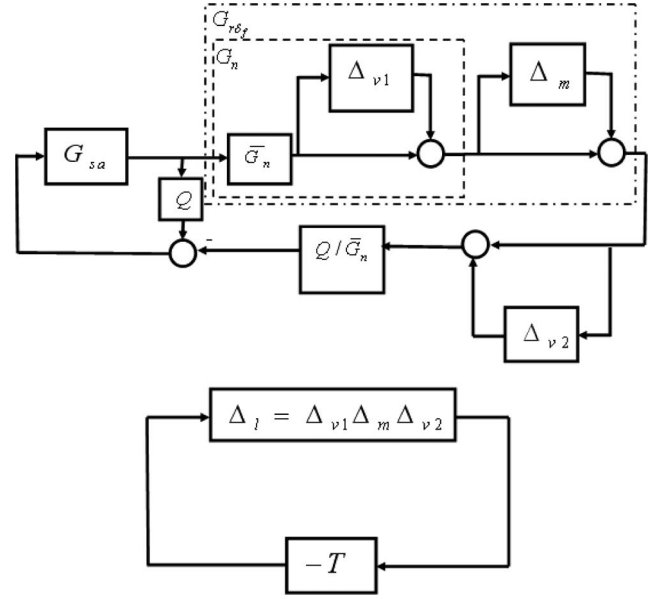

Fig. 7. LFT representation of a model regulator with multiplicative model uncertainty.

used, all deviations from the desired or nominal model G_n, like model nonlinearities, variations of parameters, etc., are treated as model uncertainty Δ_m, and, as long as they satisfy inequality (45), the robustness of stability is guaranteed.

The model regulator design requirements specified in terms of filter Q are also summarized in the magnitude Bode plot of Fig. 6. The uncertainty in (45) is treated here as uncertainty that exists due to the imprecise knowledge of parameters in the linear model like speed v, road friction coefficient μ (see Fig. 4), etc. The uncertainty in Fig. 4 was divided into an equally spaced grid of values in both axis directions, and corresponding uncertainty Δ_m from the nominal condition chosen as $\mu = 1$ and $v = 30$ m/s was obtained for each value in this grid. The inverse of the resulting $\Delta = G_{sa}\Delta_m$ plots is shown in Fig. 6 for checking stability robustness condition (45).

To be less conservative when the model uncertainty has structure, structured singular value (SSV) analysis can be used. For the linear vehicle model with varying speed, the varying speed and the road friction coefficient can be treated as uncertainty, and SSV analysis can be performed to guarantee that the stability for a maximum SSV value will be less than unity, as detailed in [22] and [23].

The small gain theorem (see [24] for example) can be used as a conservative stability check in cases where there is time-varying uncertainty like varying vehicle speed and nonlinearities. Along with uncertainty Δ_m in (29), desired model G_n chosen here as in (36) also has vehicle speed v as a variable parameter in two different blocks, with $G_{r\delta_f} = G_n(s,v)(1 + \Delta_m)$ and $Q/G_n(s,v)$ in the model regulator architecture in Fig. 5. These speed dependencies have to be incorporated into a larger uncertainty block Δ_l, as shown in Fig. 7. The desired model is separated into velocity-independent part $\bar{G}_n$ and velocity-dependent uncertainty Δ_{v1} as

$$G_n = \bar{G}_n(1 + \Delta_{v1}), \quad \bar{G}_n := G_n|_{v=30 \text{ m/s}}. \quad (46)$$
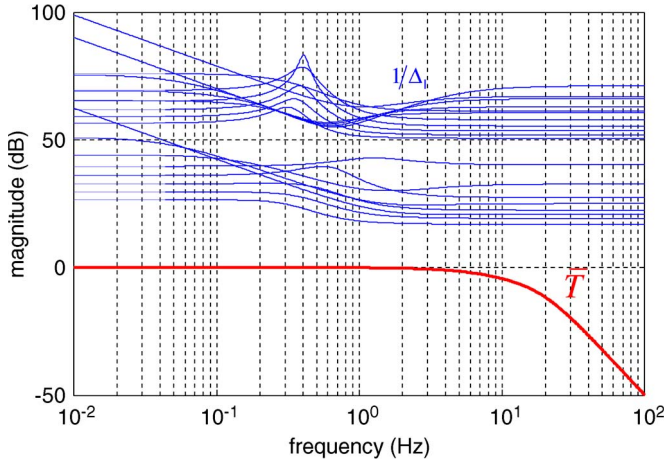
Fig. 8.   Small gain theorem check.

Using the choice of G_n in (36) results in the following:

$$\Delta_{v1} = \frac{G_n - \bar{G}_n}{\bar{G}_n} = \frac{K_n(v)}{\bar{K}_n} - 1, \quad \bar{K}_n := K_n(v)|_{v=30 \text{ m/s}}. \tag{47}$$

Similarly

$$\frac{Q}{G_n} = \frac{Q}{\bar{G}_n}(1 + \Delta_{v2}) \tag{48}$$

which, for choice (36) for G_n, results in

$$\Delta_{v2} = \frac{\bar{K}_n}{K_n(v)}1. \tag{49}$$

The model regulator with the velocity-dependent uncertainty blocks Δ_{v1} and Δ_{v2} and its equivalent linear fractional transformation (LFT) representation are shown in Fig. 7. $\bar{T}$ is the complementary sensitivity function with plant $G_{r\delta_f}$ and desired model G_n both replaced by $\bar{G}_n$ in (46). According to the small gain theorem

$$\|\Delta_l\|\| - \bar{T}\| < 1, \quad \text{or} \quad |\bar{T}| < \frac{1}{|\Delta_l|} \quad \forall \omega \tag{50}$$

where $\Delta_l = \Delta_{v1}\Delta_m\Delta_{v2}$, as shown in the bottom part of Fig. 7, and

$$\bar{T} = \frac{G_{sa}\bar{G}_n Q}{\bar{G}_n \left((1 - G_{sa}Q) + G_{sa}Q\right)} \tag{51}$$

is a sufficient condition for stability provided that the nominal closed-loop system with $\Delta_l = 0$ is stable. Note that the small gain theorem applies to time-varying uncertainty Δ_l in (50). The time-varying nature of Δ_l is due to the vehicle speed being time varying. The determination of a worst-case lower bound on $1/|\Delta_l|$ is, thus, sufficient to check (50). Note also that a single-input–single-output formulation is used in this paper. Velocity-dependent uncertainties Δ_{v1} and Δ_{v2} are evaluated along with the Δ_m computation based on the grid method mentioned earlier to obtain the $1/\Delta_l$ and $\bar{T}$ magnitude frequency responses in Fig. 8. Stability is guaranteed since inequality (50) is satisfied.
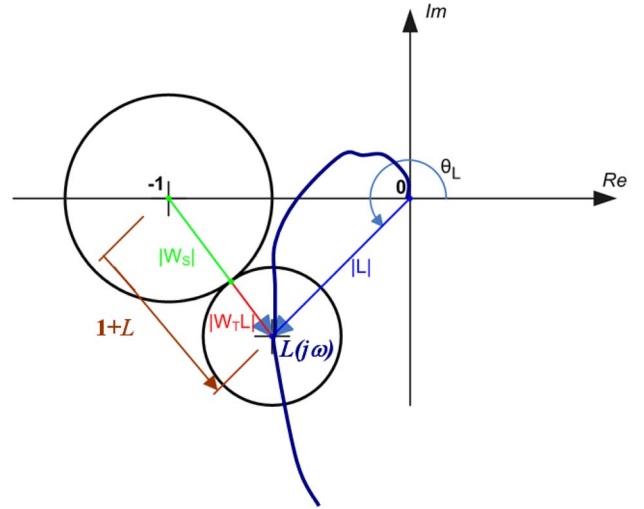

Fig. 9.   Point condition for mixed sensitivity.

V. ROBUST STEERING MODEL REGULATOR DESIGN

Similar to the approach in [25], a parameter space design based on satisfying the robust performance requirement

$$\||W_S S| + |W_T T|\|_\infty < 1 \tag{52}$$

or equivalently satisfying

$$|W_S S| + |W_T T| < 1 \quad \forall \omega \tag{53}$$

is used here. See [16] and [25] for additional information on the parameter space approach to robust control and [27] for additional information on mapping mixed sensitivity performance bounds to controller parameter space for standard feedback control structure. The inverse of the sensitivity function weight is chosen as

$$W_S^{-1}(s) = h_S \frac{s + \omega_S l_S}{s + \omega_S h_S} \tag{54}$$

with $l_S = 0.2$ (i.e., less than 20% steady-state error) being the low-frequency sensitivity bound, $h_S = 4$ being the high-frequency sensitivity bound, and $\omega_S = 15$ rad/s being the approximate bandwidth of model regulation. The complementary sensitivity function weight is chosen as

$$W_T(s) = h_T \frac{s + \omega_T l_T}{s + \omega_T h_T} \tag{55}$$

where the low-frequency gain is $l_T = 0.5$, the high-frequency gain is $h_T = 1.5$ (corresponds to uncertainty of up to 150% at high frequencies), and the frequency of transition to significant model uncertainty is $\omega_T = 120$ rad/s. See [16] for additional information on weight selection.

The robust steering controller design approach is based on mapping frequency-domain constraint (53) with weights given in (54) and (55) into the plane of chosen controller parameters τ_n and τ_Q. The solution procedure that is used is explained first before presenting the results. See [16] and [25] (and references therein) for additional information on mapping frequency-domain bounds like (53) into a chosen parameter plane. Mixed
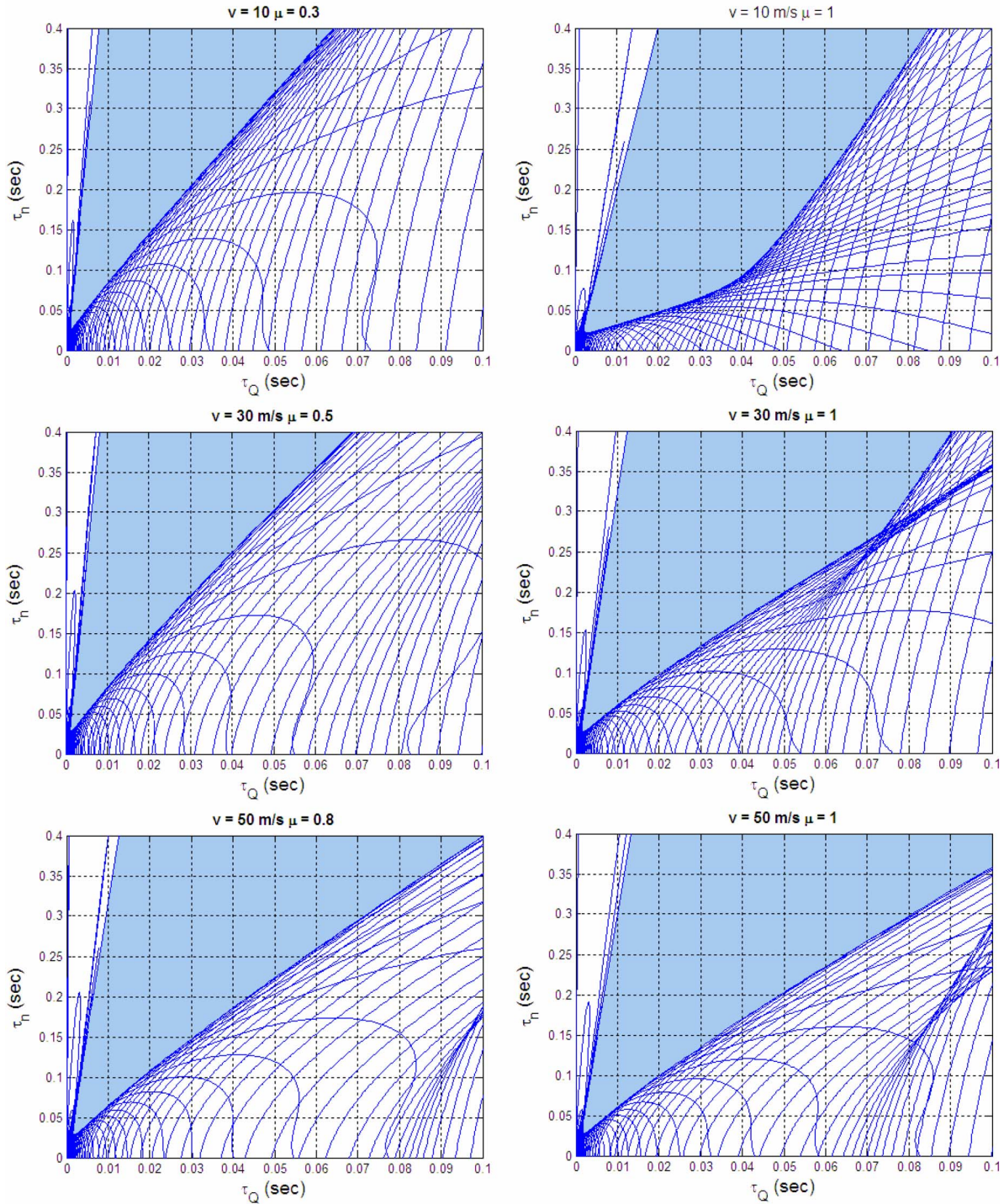
Fig. 10.   Solution region in the parameter space for each of the operating points.

sensitivity problem (53) can also be expressed in the limit as the equality

$$|W_S| + |W_T L| = |1 + L| \quad \forall \omega \tag{56}$$

which is called the point condition at each frequency. The idea is to solve (57) frequency at a time for a sufficient number of frequencies to determine regions of τ_n and τ_Q values in the $\tau_n - \tau_Q$ plane that satisfy it. The point condition is graphically illustrated in Fig. 9.

A circle with origin at -1 and a radius equal to $|W_s(\omega)|$ at a specific frequency ω is drawn first. Loop gain $L(j\omega)$ at the same frequency is shown as vector L with magnitude $|L|$ and angle θ_L in Fig. 9 and is given by

$$L(j\omega) = |L| e^{j\theta_L}. \tag{57}$$

A second circle with origin at $L(j\omega)$ and with a radius equal to $|W_T(\omega)L(j\omega)|$ for specific frequency ω being considered is drawn next.

The vector shown as $1 + L$ originating at -1 and ending at L in Fig. 9 should be greater in length than $|W_s| + |W_T L|$ to satisfy the inequality version of the point condition of (56). The touching of the tip of the peripheries of the two circles in Fig. 9 corresponds to the limit of achieving condition (56). This point condition needs to be solved at each frequency to find the controller parameter pairs that satisfy it. Solving and graphically intersecting the solution regions for a sufficiently large number of frequencies result in the controller parameter space where nominal performance is satisfied.

A graphical solution for $|L|$ using the cosine rule in Fig. 9 results in

$$|L| = \frac{-\cos\theta_L + |W_S||W_T| \pm \sqrt{\text{Disc}}}{1 - |W_T|^2} \quad (58)$$

where

$$\text{Disc} = 1 + \cos^2\theta_L - 2|W_S||W_T|\cos\theta_L + |W_S|^2 + |W_T|^2. \quad (59)$$

The first part of the solution procedure for loop gain L is the formation of a grid of θ_L in $(0{:}2\pi)$ and then solving (58) for $|L|$ and computing $L = |L|e^{j\theta_L}$. Then, L is expressed in terms of a fictitious controller K as follows:

$$L = KG_{r\delta_f} = (K_R + jK_I)G_{r\delta_f}. \quad (60)$$

Solving (60) for the real and imaginary parts K_R and K_I of the fictitious controller K and then solving

$$K_R + jK_I = \frac{G_{sa}Q}{G_n(1 - G_{sa}Q)}$$
$$= \frac{G_{sa}(j\omega)[\tau_n j\omega + 1]}{K_n(v)[\tau_Q j\omega + 1 - G_{sa}(j\omega)]} \quad (61)$$

for τ_n and τ_Q while assuming $G_{sa} = 1$ result in

$$\tau_n = -\frac{K_R}{K_I \omega} \quad (62)$$

$$\tau_Q = -\frac{1}{K_n(v)K_I\omega} \quad (63)$$

which is the final step in the solution. Determination of explicit formulas like (62) and (63) makes programming for parameter plane solution region computation easier, and the computation program written for it runs quite fast.

As part of a multiobjective approach, this solution procedure is repeated for all six of the marked operating conditions in Fig. 4. The solution region for each of the six operating conditions can be seen in Fig. 10. An interactive MATLAB program with a graphical user interface was prepared by the authors for determining parameter space regions corresponding to chosen frequency-domain criteria. The controller parameters are chosen as $\tau_n = 0.15$ s and $\tau_Q = 0.02$ s and correspond to a point within the solution regions for all six operating points. These controller parameters were used in all of the simulations reported in this paper. The $|W_S S| + |W_T T|$ frequency-domain plot for all six operating points in Fig. 4 and with the chosen controller parameters is shown in Fig. 11 as a function of
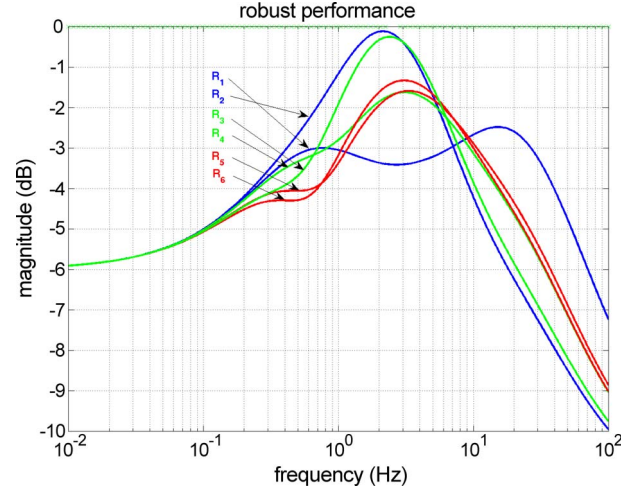

Fig. 11. Robust performance plots for each operating point.

frequency. The six different curves in this plot correspond to the six different operating points in Fig. 4. It is clear from this figure that constraint (53) is satisfied at each of the different operating points in Fig. 4 and for the chosen controller parameters, as none of the plots touch the 0-dB ($|W_S S| + |W_T T| = 1$) line.

The point condition solution procedure explained above is outlined below.

A1) Choose a specific ω value. $|W_S(\omega)|$, $|W_T(\omega)|$, and $G_r\delta_f(j\omega)$ at frequency ω are all known at this point.

A2) Let $\theta L \in [0 : 2\pi]$. Evaluate Disc using (59), and select the active range of θ_L, where Disc ≥ 0 is satisfied. For all values of θ_L in the active range

A2a) Evaluate $|L|$ using (58). Keep only the positive solutions (since $|L|$ cannot be negative).

A2b) Evaluate $L = |L|e^{j\theta_L}$.

A2c) Solve for the corresponding fictitious controller real and imaginary parts K_R and K_I in (60).

A2d) Substitute for K_R and K_I into the right-hand sides of (62) and (63), and solve for τ_n and τ_Q.

A3) Plot the closed curve of τ_n versus τ_Q values (for all active θ_L values in A2). Either the inside or the outside of this curve is a solution of (56) at chosen frequency ω. The region that is obtained is the point condition solution in the chosen controller parameter plane at the frequency chosen in step A1.

A4) Go back to step A1, and repeat the procedure at a different frequency.

A5) Plot the intersection of all point condition solutions for all frequencies considered. This is the overall solution region for robust performance.

The parameter space design used guarantees the global stability of the control structure, and the linear model used as the controller parameter space solution regions presented in Fig. 10 also includes Hurwitz stability. Global stability analysis with the full-vehicle model is not attempted, as the full-vehicle model is highly nonlinear. The actual vehicle is even more nonlinear with actuator saturation. Therefore, global stability analysis for the full-vehicle model is not practically meaningful.
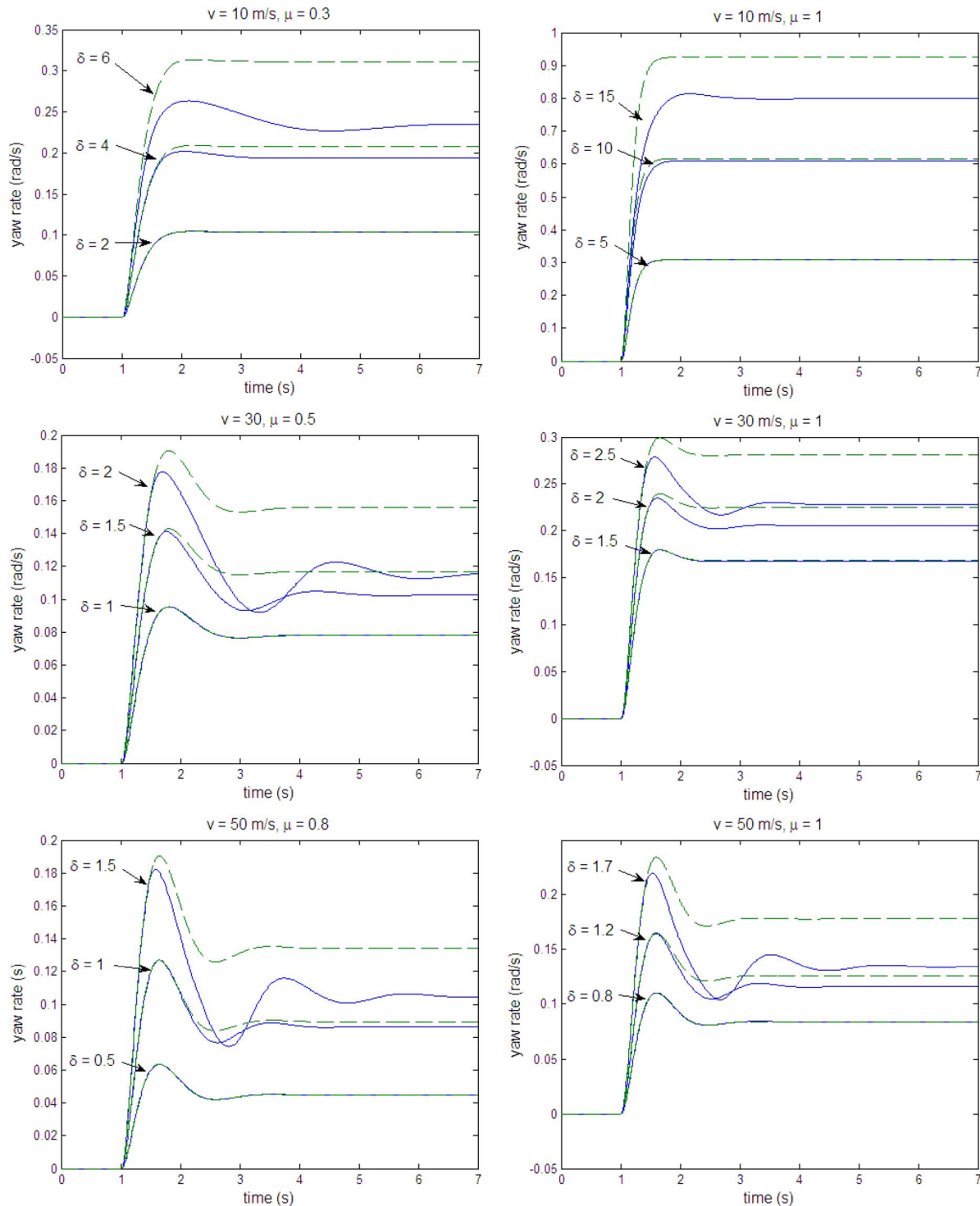
Fig. 12. Simulation results indicating an extreme maneuver for six operating points. (Dashed green line) Linear single-track model. (Solid blue line) Full model. δ is the front-wheel steering angle.

VI. SIMULATION STUDY

The simulations for step steering inputs for the linear single-track model and the nonlinear full-vehicle model are given for normal and extreme maneuvering conditions in Fig. 12. The dashed lines show the response of the linear single-track model, and the solid lines show the response of the full-vehicle model. The simulation results shown are for all six of the operating points in Fig. 4. Three different front steering-wheel angles are used for each of the operating points. Some observations based on the results in Fig. 12 are as follows: 1) For small steering angles, linear single-track and full-vehicle model responses are similar, and 2) the steering angle beyond which differences between the two model responses start is smaller for a higher vehicle speed and a lower road–tire friction coefficient. For small steering-wheel angles, the full-vehicle model is seen to behave very much like the linear single-track model. However, it is also seen in the simulations in Fig. 12 that, for each operating point,
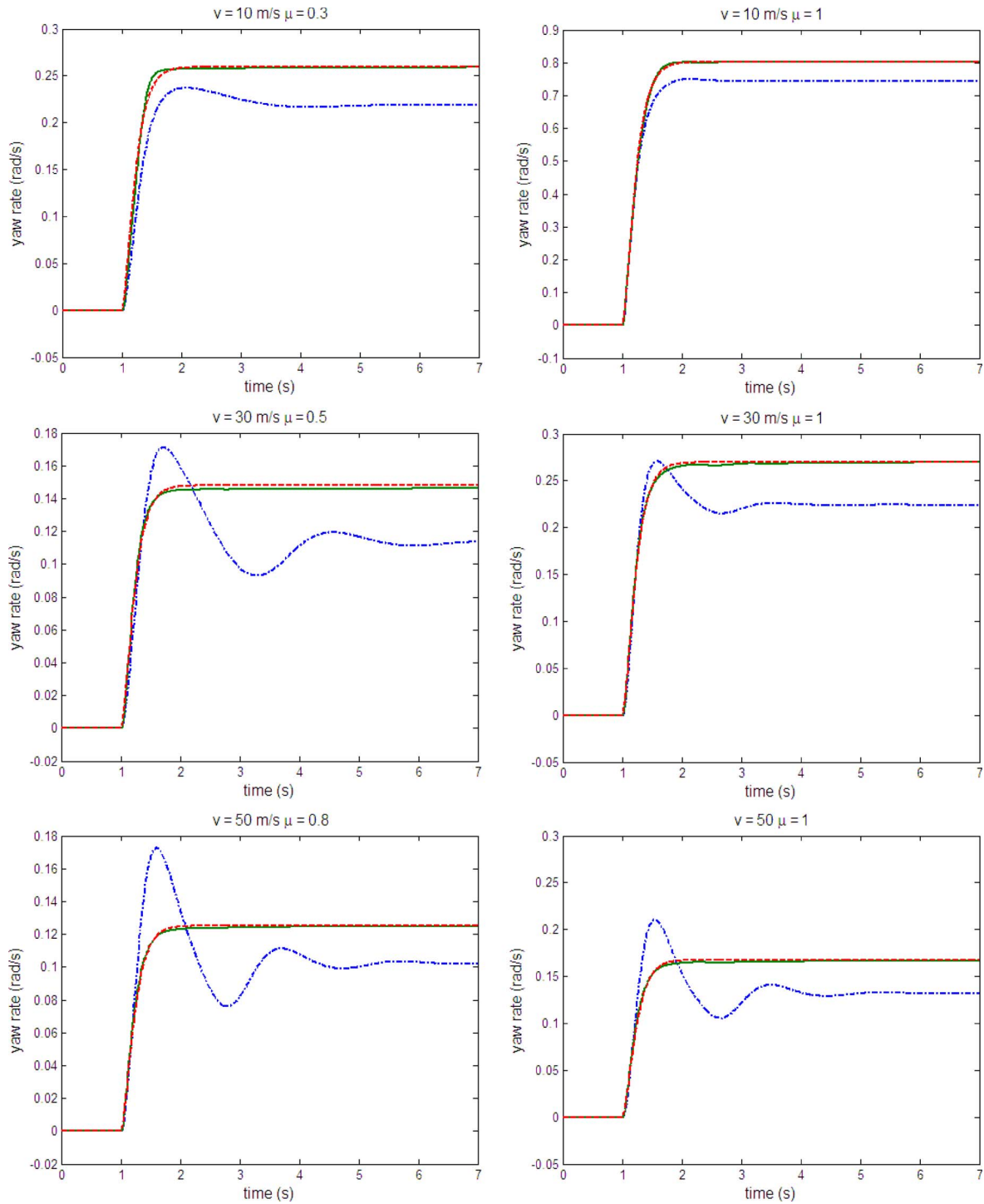
Fig. 13.   Simulation results for a step steering input. (Continuous green line) Controlled. (Dash-dotted blue line) Uncontrolled. (Dashed red line) Desired.

there exists a steering-wheel angle for which the full-vehicle model yaw rate output starts to significantly differ from the yaw rate output provided by the linear single-track model. The former condition where the linear single-track model and the nonlinear full-vehicle model yield approximately the same output is referred as a normal steering condition in this paper. In this sense, since the driver is used to the linear dynamics for normal driving conditions, we call the maneuvers with unexpected yaw rate outputs as extreme. For such maneuvers, the driver experiences the unexpected nonlinear dynamics of the vehicle.

A simulation study with the controlled and uncontrolled full-vehicle model was performed next to assess the time-domain performance that is achieved by the incorporation of the model regulator-based steering controller. Steering-wheel and yaw disturbance step inputs are the two simulation maneuvers that were investigated. Simulation results shown in Figs. 13 and 14 demonstrate the achievement of good steering command tracking and excellent disturbance rejection, respectively, at all six operating points. Model regulator steering controlled yaw rate responses in Fig. 13 are very close to the desired linear
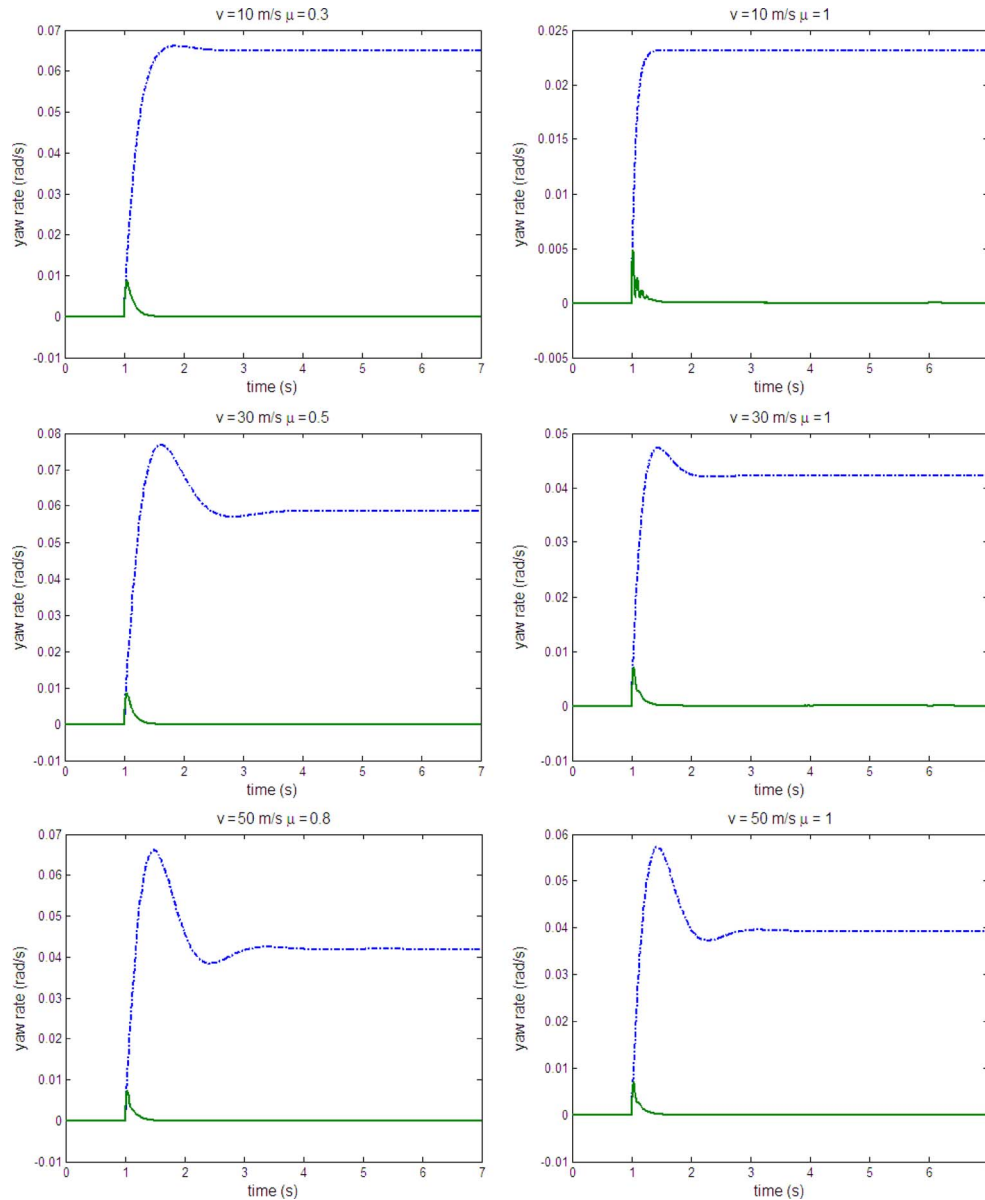
Fig. 14. Simulation results for yaw moment disturbance input. (Continuous green line) Controlled. (Dash-dotted blue line) Uncontrolled.

single-track model responses, whereas the uncontrolled steering responses are far off. The undesired yaw moment disturbance results in Fig. 14 show excellent disturbance rejection being achieved in the case of the model regulator steering controller. Steering angle input for each operating point was chosen to be the extreme maneuver as described above, and a yaw moment disturbance of 800 N · m was used in the simulations. The steer-by-wire actuator did not reach its saturation limits during the simulations. The controller output is also presented in Fig. 15 for different step steering inputs operating in $v = 30$ m/s and $\mu = 0.5$. The controller response imposing linear dynamics to the vehicle can be observed from this figure.

The simulation response with a desired velocity profile linearly ranging from 10 to 50 m/s displayed in Fig. 16 is used to evaluate the gain scheduling feature of the model regulator type steering controller presented in this paper. In this simulation, a step steering input (starting at 4 s) followed by a step yaw torque
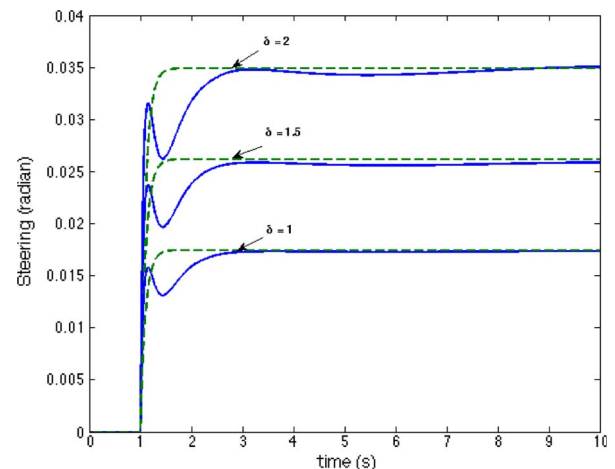

Fig. 15. Controller output for $v = 30$ m/s, $\mu = 0.5$. (Continuous blue line) Controller output. (Dash-dotted green line) Driver steering input. δ is the front-wheel steering angle (in degrees).
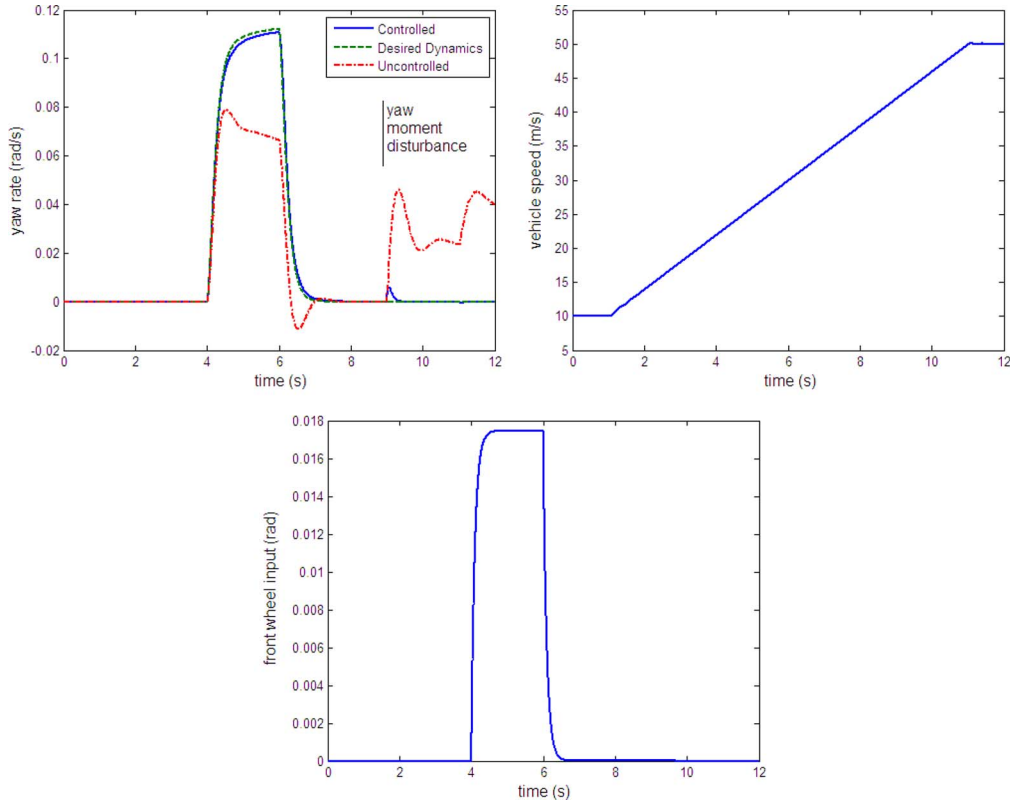
Fig. 16.   Simulation results for linearly varying vehicle speed.

disturbance input (starting at 9 s) are imparted to the system during its speedup phase. The results in Fig. 16 demonstrate good command following and excellent disturbance rejection (look at the responses around 9 s) during this variable velocity maneuver. The dynamics of the uncontrolled vehicle under the same inputs is shown in the figure as well, indicating the enhanced yaw dynamics.

The controller design process was based on the linearized tire dynamics; however, in the extreme maneuvering case, tires generally operate in the nonlinear region. For a step $2°$ steering input when the longitudinal velocity is 30 m/s and the friction coefficient is 0.5, the sideslip angle and the lateral tire force for one of the front wheels are shown in Fig. 17. Looking at the sideslip angle variation, one can observe that the tire dynamics gets close to its nonlinear region, where the lateral tire force starts to saturate. Note that the Dugoff tire model that is used in the simulations includes the coupling between the lateral and longitudinal tire forces and tire force saturation. The limit of the proposed steering controller will be reached at high sideslip values, which reduce the maximum available lateral force. Note that steering control will not work very effectively for yaw stabilization when the lateral tire force saturates. Combined differential braking plus steering control will be more effective in that case.

The simulation results demonstrate that the model regulator-based steering controller follows the desired yaw rate behavior even under extreme driving conditions, as seen in Fig. 13. The simulations also reflect the excellent disturbance rejection property of this controller, as seen in Fig. 14. Finally, it is also indicated by the simulations that the velocity-scheduled controller appropriately works for varying velocity, as seen in Fig. 16.
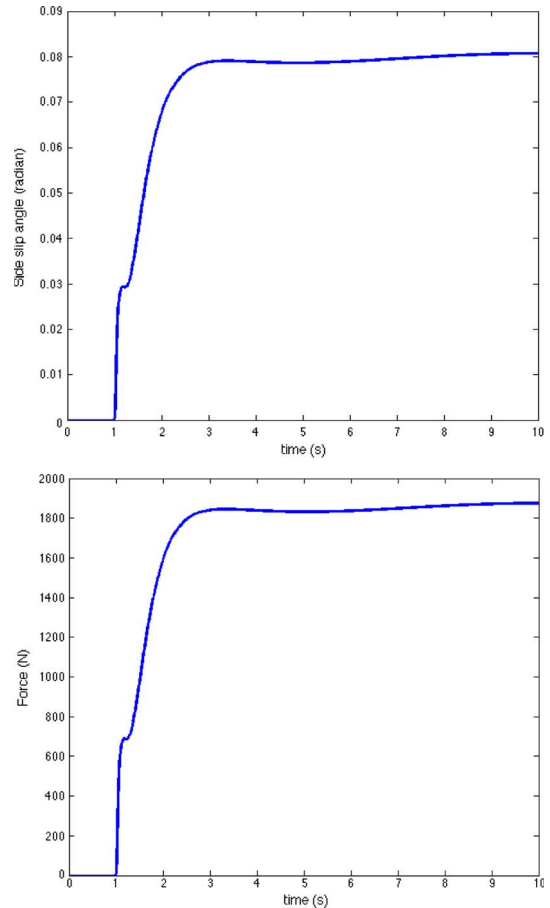

Fig. 17.   Sideslip angle and tire force plots for step steering input $v = 30$ m/s, and $\mu = 0.5$.
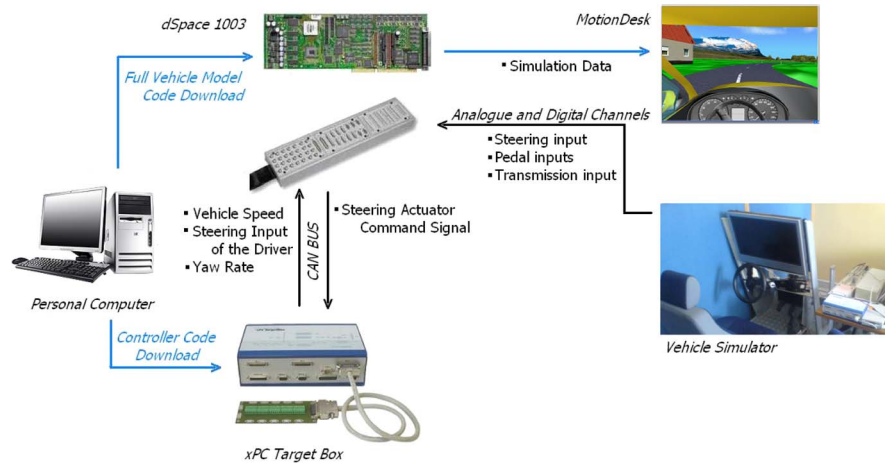
Fig. 18.   Architecture of the hardware-in-the-loop test setup.

Fig. 19.   Hardware-in-the-loop test setup.

VII. HARDWARE-IN-THE-LOOP SIMULATION SETUP

To better demonstrate the performance and the effectiveness of the proposed controller, a real-time hardware-in-the-loop simulation setup, including a human driver, was prepared. Similar hardware-in-the-loop simulation systems that are used to evaluate vehicle stability control-system performance are available in [28] and [29]. The architecture of the setup that is developed and used here is displayed in Fig. 18, and a photograph of the setup is presented in Fig. 19. In the hardware-in-the-loop test setup, the full-vehicle model ran on a dSpace DS 1103 simulator system, whereas the controller was implemented on an xPC Target Box. The communication between the controller (xPC Targetbox) and the vehicle (DS 1103) was carried out using the controller area network (CAN) bus, which is the actual bus from which the electronic control unit obtains sensory information in currently available vehicle control systems. The yaw rate sensor data, the steering input of the driver, and the vehicle speed can be acquired by the controller, and the steering actuation command can be sent to the vehicle dynamics simulator over this CAN bus.

The driver is connected to the vehicle dynamics simulator with a driver steering wheel, the pedal inputs, and a stick shift for the transmission input. All these inputs were mechanically implemented and electronically provide the sensory outputs

through either analog or digital outputs. These driver inputs are connected to the dSpace DS 1103 unit through its analog and digital channels that directly connect them to the vehicle model. The visualization for the driver is handled using the dSpace Motion Desk software. Using this software, 3-D simulation of the environment was easily implemented and was displayed on the liquid crystal display screen in front of the driver. An approximately 30-km stretch of a real road in Istanbul with highway and inner city parts is also being adapted for this simulator.

In the proposed control system, the driver inputs the steering-wheel command to the vehicle simulator. This command first flows into the vehicle simulator, and then, it is made available on the CAN bus. This operation corresponds to the simulation of a steering-wheel sensor. The control system acquires this steering-wheel input together with the yaw rate and vehicle speed data from the CAN bus and transmits the actual steering input to the actuator. The steering actuator command is acquired by the vehicle simulator, and the vehicle dynamics is simulated according to the actuator inputs. Finally, the vehicle dynamics simulator outputs the required data for visualization, and the vehicle is visualized together with the environment for the driver, placing him/her in the loop. This simulation forms a loop, including the controller hardware, the driver, and the vehicle. To demonstrate the effectiveness of the controller, the results of a hardware-in-the-loop test run are given in Fig. 20. Four different tests are presented in this figure. The controlled vehicle dynamics is observed to track the desired dynamics in the simulations. The same steering-wheel input was applied to an uncontrolled vehicle, and the results were provided in the same figure. The nonlinear dynamic effects, which the driver does not expect during these maneuvers, are obvious.

The vehicle yaw stability was shown to be enhanced, and the handling qualities were shown to be improved by the use of the model regulator steering controller of this paper in the hardware-in-the-loop tests. Simulations were carried out with controlled and uncontrolled vehicles, and the effect of the maneuvers used on the driver was observed. Throughout the simulations, the dynamics of the vehicle tracked the desired
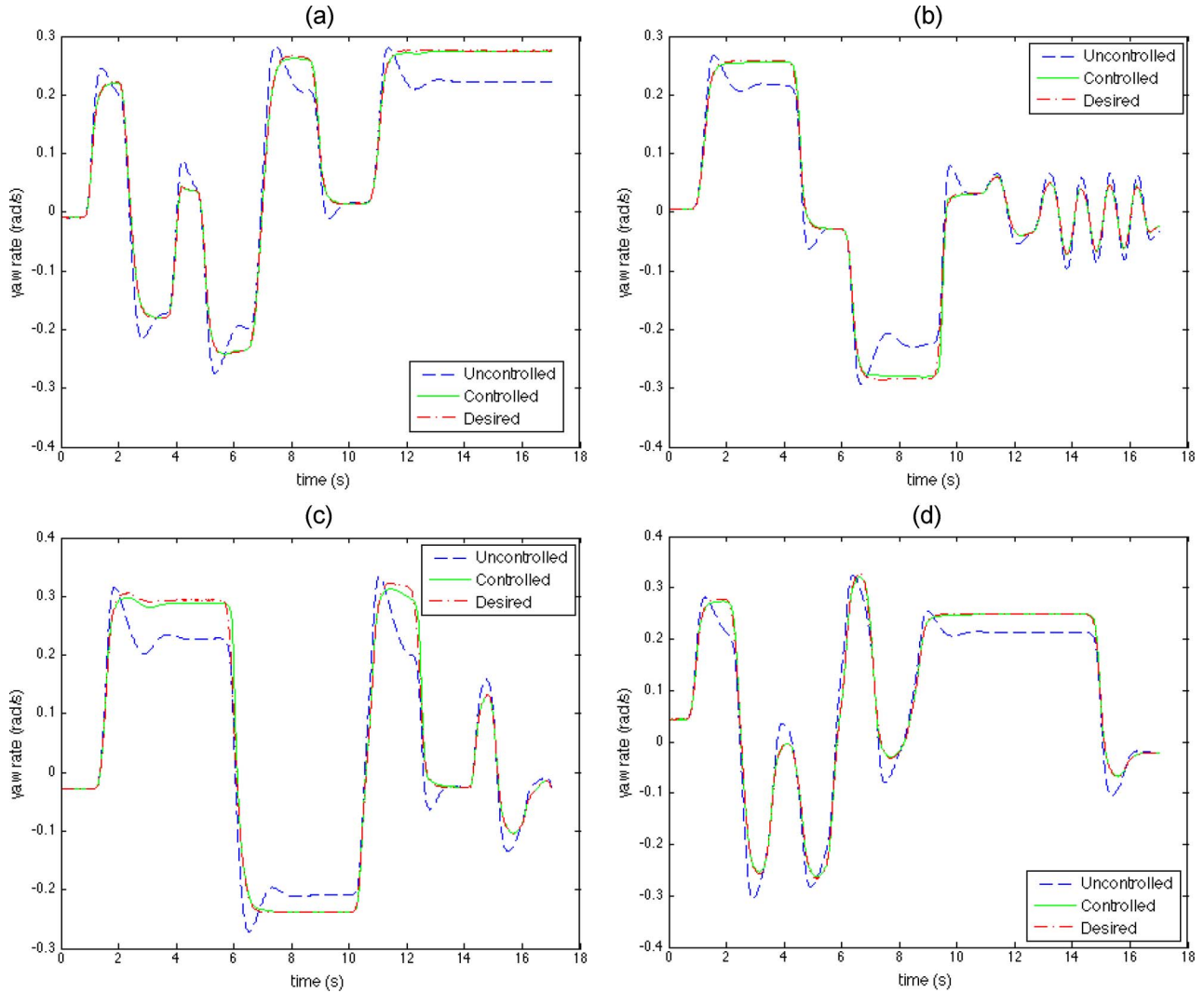
Fig. 20. Hardware-in-the-loop simulation result of the control system with a real driver. (a) Double-lane change followed by a sharp turn. (b) Single-lane change followed by several fast turns. (c) Several lane change maneuvers. (d) Fast double-lane change followed by a sharp long turn.

dynamics well. Since these dynamics were the linear dynamics that the driver is used to under normal steering conditions, several extreme maneuvers were easily performed by the driver that improved the vehicle-handling qualities under extreme conditions.

With this hardware-in-the-loop simulation setup, other kinds of vehicle control systems can also be tested in real time, including a real driver in the loop. The hardware-in-the-loop simulation setup is able to demonstrate the control system performance and give indications on vehicle-handling qualities when used with experienced drivers. Although some control systems may tend to impose much better control over the vehicle dynamics and provide safer operation, they may significantly reduce the vehicle's handling qualities. This is an important disadvantage for the end user. Testing of the vehicle-handling quality for control systems involving inputs from the driver is essential. These kinds of control systems include ABS systems as well as electronic stability program systems. Many engine and driveline control systems also interact with the driver and handling qualities.

VIII. CONCLUSION

The application of a robust model regulator design, based on mapping frequency-domain criteria to controller parameter space, to the vehicle yaw stability control problem has been presented here. The application of the mixed sensitivity-type specification to robust model regulator design has been shown to result in explicit formulas for the model regulator parameters to be tuned. A design based on this approach has been presented and evaluated using a nonlinear full-vehicle model. The gain scheduling feature of the steering model regulator used has also been tested in a variable velocity maneuver. The performance and the effectiveness of the controller have been shown in hardware-in-the-loop tests with a real driver in the loop. The hardware-in-the-loop tests provide useful insight on the effect of the control system on vehicle-handling qualities. It should be noted that the steering control that has been proposed here will not work properly when the lateral tire force saturates. In such cases, the steering controller should be combined with a differential braking controller for better operation. This will be the topic of future research. The hardware-in-the-loop

simulation setup introduced in this paper can be used to test combined steering- and differential-braking-based yaw stability control systems.

REFERENCES

[1] A. T. van Zanten, "Bosch ESP systems: 5 years of experience," presented at the Society Automotive Engineers World Congr., Detroit, MI, 2000, SAE Paper 2000-01-1633.

[2] W. Xiang, P. C. Richardson, C. Zhao, and S. Mohammad, "Automobile brake-by-wire control system design and analysis," *IEEE Trans. Veh. Technol.*, vol. 57, no. 1, pp. 138–145, Jan. 2008.

[3] E. Dincmen and T. Acarman, "Enhancement of handling and cornering capability for individual wheel braking actuated vehicle dynamics," in *Proc. IEEE Intell. Veh. Symp.*, Jun. 2007, pp. 888–893.

[4] J. I. Hernandez and K. Chen-Yuan, "Steering control of automated vehicles using absolute positioning GPS and magnetic markers," *IEEE Trans. Veh. Technol.*, vol. 52, no. 1, pp. 150–161, Jan. 2003.

[5] S. Jin-Hua and X. Xin, "Estimation of equivalent input disturbance improves vehicular steering control," *IEEE Trans. Veh. Technol.*, vol. 56, no. 6, pp. 3722–3731, Nov. 2007.

[6] M. Nagai, Y. Hirano, and S. Yamanaka, "Integrated control of active rear wheel steering and direct yaw moment control," *Vehicle Syst. Dyn.*, vol. 27, no. 5/6, pp. 357–370, Jun. 1997.

[7] C. Chen and M. Tomizuka, "Lateral control of commercial heavy vehicles," *Vehicle Syst. Dyn.*, vol. 33, no. 6, pp. 391–400, Jun. 2000.

[8] A. Hac, D. Doman, and M. Oppenheimer, "Unified control of brake- and steer-by-wire systems using optimal control allocation methods," presented at the Society Automotive Engineers World Congr., Detroit, MI, 2006, SAE Paper no. 2006-01-0924.

[9] E. Dinçmen and T. Acarman, "Application of vehicle dynamics' active control to a realistic vehicle model," in *Proc. Amer. Control Conf.*, Jul. 2007, pp. 200–205.

[10] S. C. Başlamişli, I. E. Köse, and G. Anlaş, "Design of active steering and intelligent braking systems for road vehicle handling improvement: A robust control approach," in *Proc. IEEE Int. Conf. Control Appl.*, Oct. 2006, pp. 909–914.

[11] S. Ancha, A. Baviskar, and J. R. Wagner, "Ground vehicle steering systems: Modelling, control, and analysis of hydraulic, electric and steer-by-wire configurations," *Int. J. Vehicle Design*, vol. 44, no. 1/2, pp. 188–208, Apr. 2007.

[12] P. Yih and J. C. Gerdes, "Modification of vehicle handling characteristics via steer-by-wire," *IEEE Trans. Control Syst. Technol.*, vol. 13, no. 6, pp. 965–976, Nov. 2005.

[13] B. Aksun Guvenc and L. Guvenc, "Robust two degree-of-freedom add-on controller design for automatic steering," *IEEE Trans. Control Syst. Technol.*, vol. 10, no. 1, pp. 137–148, Jan. 2002.

[14] B. Aksun Guvenc and L. Guvenc, "The limited integrator model regulator and its use in vehicle steering control," *Turkish J. Eng. Environ. Sci.*, vol. 26, pp. 473–482, 2002.

[15] J. I. Hernandez and C. Y. Kuo, "Lateral control of higher order nonlinear vehicle model in emergency maneuvers using absolute positioning GPS and magnetic markers," *IEEE Trans. Veh. Technol.*, vol. 53, no. 2, pp. 372–384, Mar. 2004.

[16] J. Ackermann, P. Blue, T. Bunte, L. Guvenc, D. Kaesbauer, M. Kordt, M. Muhler, and D. Odenthal, *Robust Control: The Structural Approach*. London, U.K.: Springer-Verlag, 2002.

[17] K. A. Unyelioglu, C. Hatipoglu, and U. Ozguner, "Design and stability analysis of a lane following controller," *IEEE Trans. Control Syst. Technol.*, vol. 5, no. 1, pp. 127–134, Jan. 1997.

[18] K. Ohnishi, "A new servo method in mechatronics," *Trans. Jpn. Soc. Elect. Eng.*, vol. 107-D, no. 1, pp. 83–86, 1987.

[19] T. Umeno and Y. Hori, "Robust speed control of dc servomotors using modern two degrees-of-freedom controller design," *IEEE Trans. Ind. Electron.*, vol. 38, no. 5, pp. 363–368, Oct. 1991.

[20] C. J. Kempf and S. Kobayashi, "Disturbance observer and feedforward design for a high-speed direct-drive positioning table," *IEEE Trans. Control Syst. Technol.*, vol. 7, no. 5, pp. 513–526, Sep. 1999.

[21] L. Guvenc and K. Srinivasan, "Friction compensation and evaluation for a force control application," *J. Mech. Syst. Signal Process.*, vol. 8, no. 6, pp. 623–638, Nov. 1994.

[22] B. Aksun Güvenç and L. Güvenç, "SSV-robustness analysis of disturbance observers with active steering control application," in *Proc. 4th IFAC Symp. Robust Control Design*, Jun. 2003, pp. 431–436.

[23] B. Aksun Güvenç and L. Güvenç, "Robustness of disturbance observers in the presence of structured real parametric uncertainty," in *Proc. Amer. Control Conf.*, Jun. 2001, pp. 4222–4227.

[24] K. Zhou and J. Doyle, *Essentials of Robust Control*. Englewood Cliffs, NJ: Prentice–Hall, 1998.

[25] L. Guvenc and J. Ackermann, "Links between the parameter space and frequency domain methods of robust control," *Int. J. Robust Nonlinear Control*, vol. 11, no. 15, pp. 1435–1453, Dec. 2001.

[26] J. Ackermann, "Parameter space design of robust control systems," *IEEE Trans. Autom. Control*, vol. 25, no. 6, pp. 1058–1072, Dec. 1990.

[27] V. Besson and A. T. Shenton, "An interactive parameter space method for robust performance in mixed sensitivity problems," *IEEE Trans. Autom. Control*, vol. 44, no. 6, pp. 1272–1276, Jun. 1999.

[28] T. Chung and K. Yi, "Design and evaluation of side slip angle-based vehicle stability control scheme on a virtual test track," *IEEE Trans. Control Syst. Technol.*, vol. 14, no. 2, pp. 224–234, Mar. 2006.

[29] H. Lee, "Virtual test track," *IEEE Trans. Veh. Technol.*, vol. 53, no. 6, pp. 1818–1826, Nov. 2004.

Bilin Aksun Güvenç (M'05) received the B.S., M.S., and Ph.D. degrees in mechanical engineering from the Istanbul Technical University, Istanbul, Turkey, in 1993, 1996, and 2001, respectively.

She is currently an Associate Professor of mechanical engineering and a Member of the Mekar Mechatronics Research Lab and the Automotive Controls and Mechatronics Research Center with the Istanbul Technical University. She was the principal investigator of several automotive control projects funded by the automotive industry. Her research focuses on motion control, robust control, and automotive control systems.

Dr. Güvenç is a member of the International Federation of Automatic Control Technical Committee on Automotive Control.

Levent Güvenç (M'96) received the B.S. degree in mechanical engineering from Boðaziçi University, Istanbul, Turkey, in 1985, the M.S. degree in mechanical engineering from Clemson University, Clemson, SC, in 1988, and the Ph.D. degree in mechanical engineering from The Ohio State University, Columbus, in 1992.

Since 1996, he has been working with the Department of Mechanical Engineering, Istanbul Technical University, where he is currently a Professor of mechanical engineering and the Director of the Mekar Mechatronics Research Laboratory and the Automotive Controls and Mechatronics Research Center. His current research interests concentrate on automotive control and mechatronics, focussing on the development of active safety control systems for road vehicles, modeling and control of hybrid electric vehicles, and hardware-in-the-loop simulation.

Dr. Güvenç is a member of the International Federation of Automatic Control (IFAC) Technical Committee on Automotive Control and the IFAC Technical Committee on Mechatronics. He is the corresponding Editor for Europe and Africa of *IEEE Control Systems Magazine*.

Sertaç Karaman received the B.S. degree in mechanical engineering and computer engineering from the Istanbul Technical University, Istanbul, Turkey, in 2007 and 2008, respectively. He is currently working toward the S.M. degree with the Department of Mechanical Engineering, Massachusetts Institute of Technology, Cambridge.

His research interests include robust control, vehicle control systems, and optimization theory.